materials

Article

Modeling of Charge Injection, Recombination, and Diffusion in Complete Perovskite Solar Cells on Short Time Scales

Krzysztof Szulc [1], Katarzyna Pydzińska-Białek [2] and Marcin Ziółek [2,*]

[1] Institute of Spintronics and Quantum Information, Faculty of Physics, Adam Mickiewicz University in Poznan, Uniwersytetu Poznańskiego 2, 61-614 Poznan, Poland; krzysztof.szulc@amu.edu.pl
[2] Institute of Physics, Faculty of Physics, Adam Mickiewicz University in Poznan, Uniwersytetu Poznańskiego 2, 61-614 Poznan, Poland; katarzyna.pydzinska@amu.edu.pl
* Correspondence: marziol@amu.edu.pl

Abstract: A model of charge population decay upon ultrafast optical pulse excitation in complete, working perovskite solar cells is proposed. The equation, including charge injections (extractions) from perovskite to contact materials, charge diffusion, and charge recombination via first-, second-, and third-order processes, is solved using numerical simulations. Results of simulations are positively verified by broadband transient absorption results of mixed halide, triple-cation perovskite ($FA_{0.76}MA_{0.19}Cs_{0.05}Pb(I_{0.81}Br_{0.19})_3$). The combined analytical and experimental findings reveal the best approaches for the proper determination of the crucial parameters that govern charge transfer dynamics in perovskite solar cells on picosecond and single nanosecond time scales. Measurements from both electron and hole transporting layer sides under different applied bias potentials (zero and close to open circuit potential) and different pump fluence (especially below 5 μJ/cm^2), followed by fitting of parameters using numerical modeling, are proposed as the optimal methodology for describing the processes taking place in efficient devices.

Keywords: perovskite solar cells; charge carrier transfer; ultrafast spectroscopy

check for updates

Citation: Szulc, K.; Pydzińska-Białek, K.; Ziółek, M. Modeling of Charge Injection, Recombination, and Diffusion in Complete Perovskite Solar Cells on Short Time Scales. *Materials* **2023**, *16*, 7110. https://doi.org/10.3390/ma16227110

Academic Editors: Grzegorz Wisz, Paulina Sawicka-Chudy, Lyubomyr Nykyruy and Rostyslav Yavorskyi

Received: 16 October 2023
Revised: 3 November 2023
Accepted: 7 November 2023
Published: 10 November 2023

1. Introduction

Perovskite solar cells (PSCs) have advanced rapidly, with power conversion efficiencies (PCEs) now exceeding 25% [1]. As in most photovoltaic systems, to obtain a high photocurrent of the device, a broad absorption of the active material and efficient photoinduced charge separation to the contact materials (electrons from one side and holes from the other side, Figure 1A) are required. The charge separation in PSCs starts in the sub-ps time range. Therefore, time-resolved laser spectroscopy has to be employed for the investigation of ultrafast charge transfer dynamics [2–8]. The study of charge transfer in perovskite materials and PSCs is an important topic but also a challenging task [9–11]. In principle, the decay of the photoexcited charges in the isolated perovskite material reveals the dynamics of the internal recombination. In complete devices, it is additionally affected by both electron and hole transfer from perovskite to contact materials: electron-transporting (ETM) and hole-transporting material (HTM), respectively, the presence of which accelerates the observed charge population decay [12,13]. The quantum yields of charge transfers to ETM and HTM determine the photocurrent and efficiency of the device and depend on the competition between the charge transfer (charge injection from perovskite to ETM/HTM, often also called charge extraction) rate constants (k_{IET} and k_{IHT}, Figure 1A) and the recombination rate constants. However, under laser pulse excitation, not only the first-order recombination (trap-assisted, with rate constant k_1) takes place, but also second- (radiative, k_2) or even third-order (Auger, k_3) processes are frequently observed, and thus the apparent decay kinetics depend on the pump pulse intensity even for relatively low-intense pulses [14]. Moreover, in perovskite devices, the thickness of the active material is in the order from tens to several hundreds of nanometers, and the initial distribution of the photoexcited charges (Figure 1B) changes due to the charge diffusion process that occurs on the time scales from hundreds of picoseconds to single nanoseconds [14–16]. Therefore, the following equation for the charge population n has to be solved, in which the term with diffusion constant (D) has to be included:

$$\frac{\partial n}{\partial t} = D\frac{\partial^2 n}{\partial z^2} - (k_1 + k_{\mathrm{IET}} + k_{\mathrm{IHT}})\, n - k_2 n^2 - k_3 n^3. \tag{1}$$

The above-resultant equation can only be solved numerically to properly describe the interfacial electron- and hole-transfer dynamics and extract the charge transfer parameters. This is probably the reason why it is still rarely used in the analysis of time-resolved measurements of PSCs on the time scale from ps to ns.

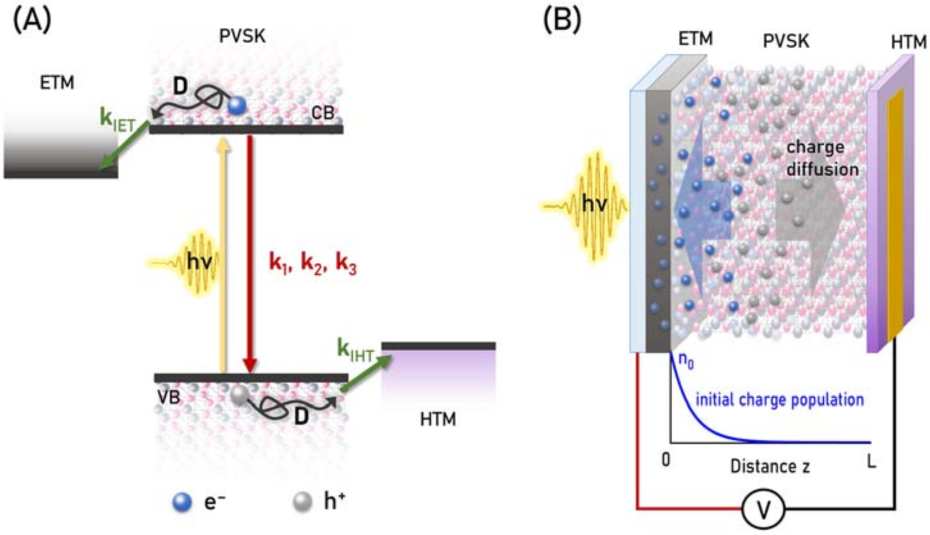

Figure 1. (**A**) Scheme of the energy levels and charge-transfer processes in PSCs. (**B**) Scheme of the configuration of PSC for the measurements under applied voltage for pulse excitation from the ETM side; bottom: initial charge distribution along perovskite thickness.

Several analytical functions are frequently used to model the decay of the charge population observed in time-resolved measurements of PSCs, and they are critically outlined below. The first one is the multi-exponential function [17,18]:

$$\Delta A(t) = A_0 + A_1 e^{-\frac{t}{\tau_1}} + A_2 e^{-\frac{t}{\tau_2}} + \cdots + A_{\mathrm{n}} e^{-\frac{t}{\tau_n}}, \tag{2}$$

with time constants τ_i related to pre-exponential factors A_i, and A_0 being an optional constant offset component. In the simplest way, the multi-exponential functions are fitted at a single wavelength (e.g., at a maximum of emission or a minimum of bleach signal in transient absorption) [17,19,20]. In broadband measurements, much more information can be gathered via global fitting in the broad spectral range [18,21–27]. In the global fitting using the multi-exponential function, the pre-exponential factors A_i in Equation (2) become wavelength-dependent and are called pre-exponential factor spectra or decay-associated spectra (DAS). Increasing the number of exponential components can result in a very good quality of fit. However, the particular time components usually do not have a certain physical meaning because almost no processes in perovskites can be described by exponential function decay. In particular, higher-order recombination and/or diffusion cannot be represented by the exponential functions.

The differences in the pre-exponential factor spectra sometimes enable us to distinguish different processes in the charge population evolution, and the corresponding time constants can be then treated as the average time scale of these processes. For example, despite poor fit quality, we used two-exponential approximation in the global analysis of broadband transient absorption data to separate charge cooling in PSCs (time-constant typically <1 ps) from the average decay of the bleach band (times from hundreds of ps to single ns) [18,21,22]. The addition of more exponential components, especially for the samples excited at relatively high pump fluence, revealed bleach decay with the bands blue-shifted for shorter time constants, confirming that the band-filling mechanism in perovskites affects the more short-wavelength transitions at shorter times [21,28]. This is one of the justifications why broadband bleach integration is necessary for the proper representation of the photoinduced charge population (see below).

Another analytical approach concentrated on the important role of second-order recombination in charge population decay. When the diffusion term and third-order recombination are neglected ($D = 0$, $k_3 = 0$), then Equation (1) can be solved analytically, leading to the so-called mixed first and second-order decay function:

$$\Delta A(t) = \frac{A\, k_1}{k_1 e^{k_1 t} - k_2 n_0 \left(e^{k_1 t} - 1\right)}, \tag{3}$$

where n_0 is the number of excited carriers at $t = 0$ and A is the proportional term. The function above is mostly employed for fitting time-resolved emission data [29–31]. However, we also tried it for transient absorption results. The fit quality was sufficient in certain cases but mostly at low excitation fluence [21]. The typical verification of this model is to check whether the first and second-order rate constants (k_1 and k_2) do not change in the fit at different excitation fluences.

Finally, the stretched-exponential function is sometimes used for fitting the charge decays in PSCs:

$$\Delta A(t) = A_0 e^{-\left(\frac{t}{\tau}\right)^{\beta}}, \tag{4}$$

with the stretched parameter $0 < \beta \leq 1$ (at lower values, the function is "spread" over more time scales). This function can describe signal decay as a distribution of sources decaying at different rates, e.g., due to diffusion. The physical meaning can have the averaged decay time (τ_{AVG}), which can be obtained as

$$\tau_{\mathrm{AVG}} = \frac{\tau}{\beta} \Gamma\left(\frac{1}{\beta}\right), \tag{5}$$

where Γ is the gamma function. Time-resolved data of PSCs are successfully fitted with the stretched-exponential function in a limited number of cases [21,22], mostly at a low pump fluence. Interestingly, we recently found an improved fit quality when the mixed first- and second-order function Equation (3) is additionally stretched ($\beta = 0.3$) [22]; however, its physical meaning is hard to explain.

It should be stressed that although all the above analytical models can offer some clues regarding the time scales of the charge transfer processes in perovskites, they cannot provide the precise values of the rate constants because the charge diffusion is not included in any of them. In particular, the interfacial charge injection rate constants that are extracted from such models are significantly smaller than the values of k_{IET} and k_{IHT} fitted in the numerical simulation of Equation (1). Therefore, in this work, we show how Equation (1) can be used to study the ultrafast and fast charge dynamics in complete PSCs (with ETM, HTM, and both electrodes) and discuss its interesting implications.

A versatile way to study fast charge population decay in PSCs is to analyze the bleach dynamics observed in transient absorption (ΔA, measured in the transmission mode) upon pulse excitation. Such transient absorption studies permit the easy collection of the decays for several pump pulse fluences, selective excitation from both ETM and HTM sides, and, as we recently showed, even the measurements through metal electrodes under an applied bias voltage [32]. In some reports about PSCs, it is assumed that single-electron injection to ETM or separate hole transfer to HTM does not contribute to bleach recovery, probably in analogy to most of the organic (molecular) systems in which the charges are localized and the simultaneous extraction of both electron and hole (from a photoinduced electron–hole pair) is necessary to observe ground state recovery (bleach decay). However, in perovskites, like in other inorganic semiconductors, the electrons and holes exist as free charges and are delocalized. Therefore, the changes in their population due to transfers to contact materials can be independently observed via bleach band decay (see Figure S1A in Supporting Information). This feature has been frequently confirmed in PSCs transient absorption studies in which the bleach decay accelerated after the addition of contact material (single ETM or HTM) with respect to pristine perovskite or by recording bleach kinetics similar to fluorescence decay [6,13,18,23,24,33].

The inclusion of the diffusion term in Equation (1) has been sometimes used in the studies of isolated perovskite materials [12,15,23,34] but very rarely in the systems with the ETMs and/or HTMs. In one of the pioneering works [16], $MAPbI_3$ perovskite of different thicknesses with the contacts of either PCBM or spiro-OMeTAD was studied, and the intrinsic interfacial electron and hole transfers were observed to be much faster than the diffusion process. Moreover, it has also been shown that electrons and holes contribute with different weights to the bleach signal [16]:

$$\Delta A(t) \propto \chi n_{\mathrm{e}}(t) + (1-\chi) n_{\mathrm{h}}(t), \tag{6}$$

where n_{e}, n_{h}—density of electrons and holes and χ—the weight of electron contribution to the bleach feature (fitted value: $\chi = 0.7$). We based our methodology on the above approach, but we extended it to the complete solar cells (with both ETM and HTM), included Auger recombination, and proposed an alternative way to correctly determine charge population based on band integral (*BI*) instead of single ΔA kinetics at bleach minimum [21].

2. Results and Discussion

Our methodology of charge-transfer modeling is described below. Equation (1) treats electrons (n_{e}) and holes (n_{h}) separately, as they exist as free charges in perovskites, offering the following set of equations used for bleach decay modeling [16,35]:

$$\frac{\partial n_{\mathrm{e}}}{\partial t} = D\frac{\partial^2 n_{\mathrm{e}}}{\partial z^2} - k_1 n_{\mathrm{e}} - k_2 n_{\mathrm{e}} n_{\mathrm{h}} - k_3 n_{\mathrm{e}} n_{\mathrm{e}} n_{\mathrm{h}} - \delta_{\mathrm{e}}(z) k_{\mathrm{IET}} n_{\mathrm{e}}, \tag{7}$$

$$\frac{\partial n_{\mathrm{h}}}{\partial t} = D\frac{\partial^2 n_{\mathrm{h}}}{\partial z^2} - kk_1 n_{\mathrm{h}} - k_2 n_{\mathrm{e}} n_{\mathrm{h}} - k_3 n_{\mathrm{e}} n_{\mathrm{h}} n_{\mathrm{h}} - \delta_{\mathrm{h}}(z) k_{\mathrm{IHT}} n_{\mathrm{h}}. \tag{8}$$

Both charge distributions n_{e} and n_{h} are the functions of time (t) and distance (z) in perovskite. Intrinsic electron and hole transfers with rate constants k_{IET} and k_{IHT} occur close to the interface (in our model, at a 1 nm distance from ETM or HTM); thus, delta functions are zero except for $\delta_{\mathrm{e}} = 1$ for $0 < z < 1$ nm and $\delta_{\mathrm{h}} = 1$ for L—1 nm $< z < L$, where L is the perovskite thickness (Figure 1B). Calculation of proper charge population requires broad spectral integration over the bleach band to take into account the bleach broadening effect due to band filling mechanism [21,22,32,36]:

$$BI(t, \Delta\lambda = \lambda_2 - \lambda_1) = \int_{\lambda_1}^{\lambda_2} \Delta A(t,\lambda)\frac{d\lambda}{\lambda}\,. \tag{9}$$

The above so-called band integral (*BI*) amplitude taken from the transient absorption measurements is thus proportional to the weighted contribution of electron and hole populations:

$$BI(t) = S\left(\chi \int_0^L n_{\mathrm{e}}(z,t)dz + (1-\chi)\int_0^L n_{\mathrm{h}}(z,t)dz\right), \tag{10}$$

where S is the scaling factor. The initial distributions of the charges are as follows (Figure 1B):

$$n_{\mathrm{e}}(z,0) = n_{\mathrm{h}}(z,0) = n_0 \exp(-\alpha z), \tag{11}$$

where $n_0 = \alpha J$, α is the absorption coefficient (in cm^{-1}), J is pump fluence (in photons/cm^2).

The simulations of the system were performed in COMSOL Multiphysics software v. 5.4 (see Section 3). The expression in the brackets of Equation (10) is called weighted surface charge distribution (WSCD) and presented as a function of time in the units of cm^{-2} in most of the figures below.

First, we validated the proposed model by comparing it with the experimental results. Figure 2 shows the representative examples for our PSCs made using the benchmark triple-cation, mixed halide lead perovskite ($FA_{0.76}MA_{0.19}Cs_{0.05}Pb(I_{0.81}Br_{0.19})_3$) with standard mesoporous TiO_2 as ETM and spiro-OMeTAD as HTM layers, showing the effects of different pump pulse fluences, different applied voltages, different excitation sides (ETM and HTM) as well as different excitation wavelengths (thus different absorption coefficients of the perovskite layer). The samples were obtained from our previous reports [28,32], and the new ones were prepared in an analogous way. The triple-cation mixed halide perovskite composition is one of the most stable perovskite formulas, especially for humidity and structural impurities, with very high PCE [37]. The *BI* over the spectral range from $\lambda_1 = 680$ nm to $\lambda_2 = 800$ nm was taken to cover the entire bleach range (including that at the initial time delays; see Figure S1B). In each part of Figure 2A–D, the fits are global in the sense that such common values of parameters are searched for which the different curves are simultaneously well reproduced. As can be seen, the agreement between the experimental data and the numerical calculations is good, e.g., the Pearson correlation coefficients for the two curves in Figure 2A are 0.997 and 0.996. The extracted parameters (diffusion coefficient and rate constants) are in the following range for the different samples in each figure (Table 1): $D = (1 \div 3) \times 10^{-2}$ cm^2/s, $k_1 = 3 \times 10^5$ s^{-1}, $k_2 = (0.8 \div 3) \times 10^{-10}$ cm^3/s, $k_3 = (0.2 \div 7) \times 10^{-28}$ cm^6/s, $k_{IET} = (1 \div 3) \times 10^{11}$ s^{-1}, $k_{IHT} = 1 \times 10^{11}$ s^{-1}; χ was fixed at a value of 0.7 based on reference [16]. These values are in general agreement with other reports for PSCs, although the time-resolved reports of the studied triple-cation perovskites are quite rare [22,32,38], so the exact comparison is difficult.

Table 1. Solar cell and charge transfer parameters of the modeling fitted to the experimental presented in Figure 2.

Parameter	Figure 2A	Figure 2B	Figure 2C	Figure 2D
Pump (side, fluence)	ETM side, 30 μJ/cm^2	ETM side, 2.5 μJ/cm^2	Both sides, 10 and 30 μJ/cm^2	HTM side, 30 μJ/cm^2
L, nm	500	500	600	500
D, cm^2 s^{-1}	3×10^{-2}	3×10^{-2}	1×10^{-2}	2×10^{-2}
k_1, s^{-1}	3×10^5	3×10^5	3×10^5	3×10^5
k_2, cm^3 s^{-1}	0.9×10^{-10}	3×10^{-10}	0.8×10^{-10}	3×10^{-10}
k_3, cm^6 s^{-1}	2.5×10^{-28}	7×10^{-28}	0.4×10^{-28}	0.2×10^{-28}
k_{IET}, s^{-1}	3×10^{11} or 0	1×10^{11} or 0	1×10^{11}	1×10^{11}
k_{IHT}, s^{-1}	-	-	1×10^{11}	-
J_{sc}, mA cm^{-2}	20	15	24	20

The high rates of intrinsic charge injections to contact material (k_{IET} and k_{IHT}, injection times in single ps range) should be highlighted, confirming that the apparent slow bleach decay over single ns is due to diffusion contribution [16]. Figure S2 presents the simulation of the distribution of the charges across the perovskite thickness at different time delays and different pump fluences, showing the interplay between charge diffusion, charge recombination, and charge injection. The necessity of the inclusion of the Auger recombination (rate constant k_3) to properly describe the experimental data should be stressed. The contribution of the third-order recombination was neglected in many of the previous time-resolved studies on PCSs at similar pump fluence. We think that it might be due to the fact that the bleach kinetics analysis has been earlier limited only to its minimum. In this way, the initial fast decay that repopulates mainly the high energetic (short-wavelength) part of the bleach spectrum is missing, and the kinetics are apparently slower. Its inclusion in the proper spectral integration (*BI*) makes the charge population decay faster [21]. Next, it can be noticed that the residual signal is smaller for the excitation from HTM than the ETM side (Figure 2C), which we previously interpreted as a possible faster hole injection to HTM than electron injection to ETM [22]. However, in the current model, the fitted injection rate constants are found to be the same (k_{IET} = k_{IHT}), and the difference occurs due to the asymmetry in the contribution of electrons and holes to bleach decay ($\chi > 0.5$). The modeled first-order recombination (k_1) is kept at low values (µs time range), so it does not contribute to the charge population decay, while for the pump fluence of several tens of µJ/cm^2, the decay is dominated by k_2 and k_3. Obviously, it leads to the acceleration of the charge population decay upon increasing the pump fluence (Figure 2C, or comparison between Figure 2A,B). Interestingly, for the samples with better photocurrent (Figure 2C), the recombination rate constants k_2 and k_3 are smaller than those for the samples with worse photocurrent (Figure 2B). Finally, tuning the excitation wavelength towards the red makes the apparent kinetics slower (with all rate constants and diffusion coefficient being the same, Figure 2D). This is because the absorption coefficient α decreases, and the initial charge distribution in Equation (11) becomes more uniformly distributed along the perovskite depth z, so the charge recombination and interfacial injection are less probable, and the lifetime of the charges increases.

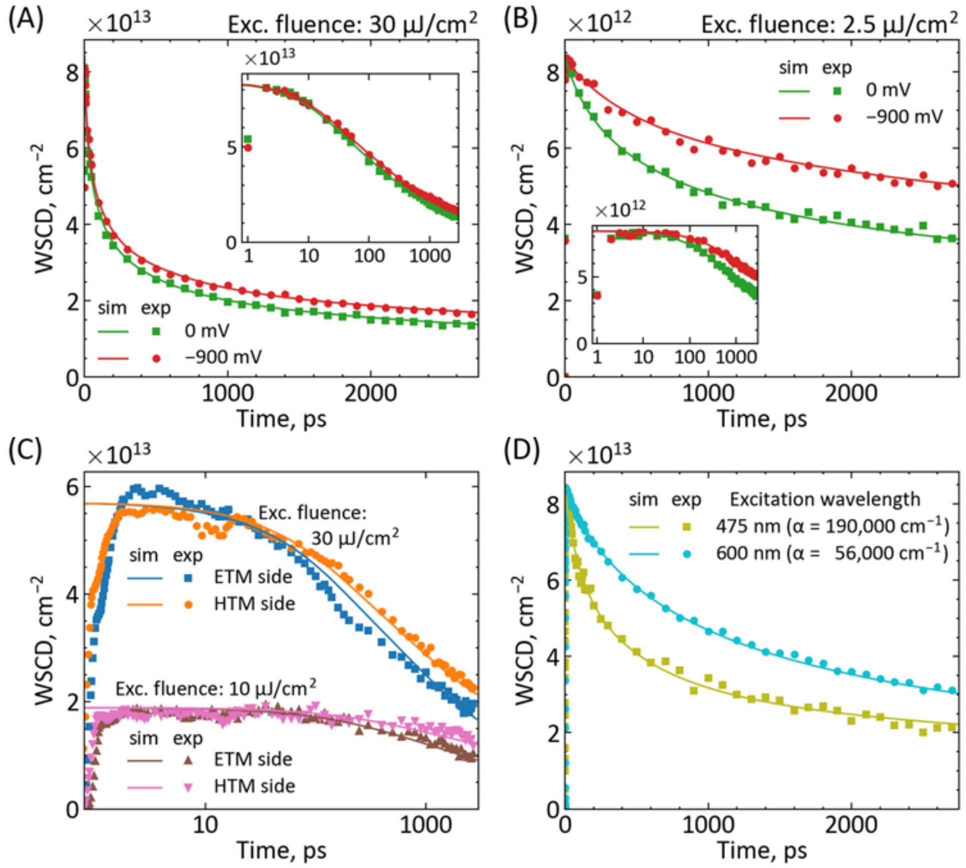

Figure 2. Comparison between the experimental results (exp, points, from *BI*) and numerical modeling (sim, lines) based on Equation (10). The solar cell and modeling fitted parameters are given in Table 1. (**A**) Our recently published experimental results for different bias potentials (0 V and −900 mV) [32]. In the latter case, the current flow is blocked, so charge injection is not possible (k_{IET} = 0 s^{-1} for −900 mV). (**B**) The new results at a lower pump fluence for 0 V and −900 mV bias potentials (k_{IET} = 0 s^{-1} for −900 mV). (**C**) The experimental results for our highest-efficiency PSC device [28] measured at two pump fluences and from both ETM and HTM sides. (**D**) The effect of pump wavelength, the excitation from the HTM side (through the gold electrodes). We note the logarithmic scale on the horizontal (time) axis in (**C**) and the insets in (**A**,**B**). The effect of possible photoinduced changes in the samples [32] was monitored and minimized.

We are aware that the model could be further extended, taking into account self-absorption (of emitted photons), additional interfacial charge recombination processes, different diffusion constants for electrons and holes, and/or distance-dependent k_1 and k_2 rate constants (different close to both interfaces) [15,22,35,38]. Moreover, drift and capacitive charging effects have been shown to be essential to model the charge decay on longer time scales, from tens of nanoseconds to microseconds (using combined drift–diffusion and Poisson equations) [39,40]. The approximation of an exponential decay of the absorption profile given by Equation (11) might not be sufficient if the perovskite thickness is smaller and/or the excitation wavelength is longer (smaller α values) than those used in our studies. Then, all excitation light will not be absorbed within the perovskite layer and additional effects due to light reflection at opposite interface and light interference should be taken into account, e.g., using transfer matrix methods [41,42]. The mixed halide perovskite that we used in our studies might also suffer from photoinduced ion migration that can be a source of additional cation-mediated recombination and affect the charge transfer kinetics and hysteresis of the cells [43,44]. We have recently observed the photoinduced changes in transient absorption spectra and kinetics for our triple cation mixed halide samples when the transient absorption experiment lasted more than several minutes [32]. Therefore, the experimental results modeled in the current studies were obtained from short-time measurements of fresh samples when the ion-migration effects could be neglected. We also do not consider the possible electron or hole injections during sub-ps charge cooling and accompanying exciton dissociation processes. However, for the examples tested by us so far, the agreement with the experimental data is sufficient on a time scale from single ps to single ns, while adding more parameters makes the fitting more complicated and less unequivocal.

Our current model enables us to reveal several interesting and apparent relationships between the parameters, which we discuss below based on the performed additional simulations. Figures 3, S3 and S4 show the results of the simulated parameter variations. We performed it for a 475 nm excitation (α = 190,000 cm^{-1}) at two pump pulse fluences: high (30 $\mu\mathrm{J/cm}^2$) and low (2.3 $\mu\mathrm{J/cm}^2$), corresponding to $n_0 = 1.3 \times 10^{19}$ cm^{-3} and $n_0 = 0.1 \times 10^{19}$ cm^{-3}, respectively, which represent the experimental conditions from Figure 2. The initial values of the diffusion and rate constant parameters are also similar to those determined from the above fits to the experimental *BI* decays.

First, it should be noticed that at a short-wavelength excitation (<500 nm) and the perovskite thickness $L > 500$ nm, there is no influence of the further L increase on the charge population kinetics (up to 3 ns, which is the temporal window of our setup; Figure 3A) and it is independent from the charge injection to the opposite side contact material. For example, for the excitation from the ETM side, the kinetics become faster with increasing the electron injection rate constant (for $k_{\mathrm{IET}} > 1 \times 10^9$ s^{-1}, Figures 3B and S4D–F) while they do not change at all for any variation of the hole injection rate constant (k_{IHT}, Figure S4G–I). The situation is fully symmetric on the HTM side (no influence of k_{IET}); only the residual signal is different if χ is different from 0.5. It confirms that one can probe selectively different contacts (ETM and HTM) by the excitation from different sides of the perovskite, which is a great advantage of femtosecond transient absorption setups over many other techniques for PSC characterization.

Next, for high pump pulse fluence (>5 $\mu\mathrm{J/cm}^2$), the dominant contribution to the charge population decay comes from the second-order (k_2) and even third-order (k_3) recombination (Figures 3C and S3H,I,K,L) and the effect of k_{IET} (or k_{IHT}) variation is small (Figure 3B). For 30 $\mu\mathrm{J/cm}^2$, the residual signal at 3 ns is greatly dependent on k_2 values, while k_3 modifies the kinetic profile at short times (tens of ps)—see Figure S3H,I,K,L. On the contrary, at lower fluence, the kinetics significantly depend on the interfacial charge injection rate constants (Figure 3B), the contribution of k_2 is decreased (Figure S3G), while the effect of k_3 is marginal (Figure S3J). This suggests that the possibility of extraction of the precise values of charge injection rate constants (k_{IET} and k_{IHT}) is limited under high pump fluence. Thus, longer-lasting transient absorption experiments at lower pump fluencies are necessary. However, a decrease of the pump fluence much below 1 μJ/cm^2 does not have much effect on the kinetics, since higher-order recombination is already significantly suppressed below 5 μJ/cm^2 (Figure 3C). It can also be noted that first-order recombination starts to offer some contribution to the simulated decays for values k_1 = 10^8 s^{-1} or higher (Figure S3D–F).

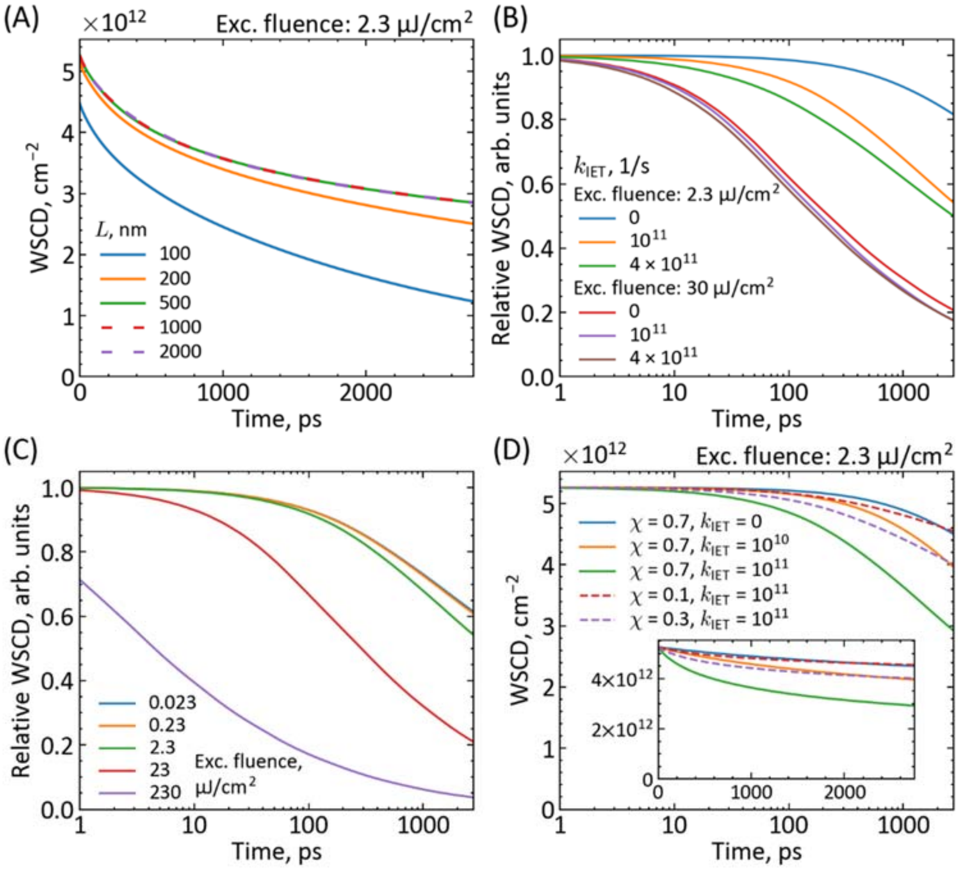

Figure 3. Simulations of charge population decay observed in transient absorption of PSCs (calculated from Equation (10)) for different parameter variations: (**A**) perovskite thickness, (**B**) electron injection rate constant, (**C**) pump fluence, (**D**) electron injection rate constant and electron contribution to the bleach. If not otherwise indicated in the graph insets, the values of the parameters in the simulations are as follows: L = 500 nm, χ = 0.7, $D = 2 \times 10^{-2}$ cm^2/s, $k_1 = 1 \times 10^5$ s^{-1}, $k_2 = 2 \times 10^{-10}$ cm^3/s, $k_3 = 2 \times 10^{-28}$ cm^6/s [0 for (D)], $k_{IET} = k_{IHT} = 1 \times 10^{11}$ s^{-1}, α = 190 000 cm^{-1} (475 nm excitation from the ETM side). Pump fluence of 2.3 μJ/cm^2 corresponds to $n_0 = 0.1 \times 10^{19}$ cm^{-3}.

Furthermore, at certain pump fluence, the increase in the residual value of the *BI* kinetics (at 3 ns) can be realized via the variation of the weight of electron contribution (χ) or the variation of interfacial injection rate constant (e.g., k_{IET} for the excitation from the ETM side). Figures 3B, S3A and S4D show examples of the population decay for several values of these two parameters at low pump fluence. Therefore, as we mentioned before, a simple comparison of the residual values for the excitation at ETM and HTM sides cannot unambiguously lead to the comparison of electron and hole injection rates (Figure 2C). For example, Figure 3D shows that for the excitation from the ETM side, the same increase in residual value is realized when k_{IET} drops from 1×10^{11} s^{-1} to 1×10^{10} s^{-1} or when χ decreases from 0.7 to 0.3. However, the shape of kinetics is different when the residual value increases due to the change in k_{IET} (faster initial decay) or due to the change in χ (slower initial decay). Thus, with a sufficient signal-to-noise ratio of the experimental data, the fit of our model should distinguish these two cases.

Nevertheless, we propose that the most reliable method for k_{IET} and k_{IHT} determination is transient absorption measurements without and with applied forward bias voltage (at the value close to the open circuit voltage of the cell, V_{OC}, so there is no current flow in the cell) and exciting the cells from ETM and HTM sides to determine separately k_{IET} and k_{IHT}, respectively. In this case, one can be sure about the same perovskite morphology and properties both with charge injections ($k_{\text{IET}} > 0$ or $k_{\text{IHT}} > 0$) and when these processes are blocked by bias forward voltage of about V_{OC} (then $k_{\text{IET}} = k_{\text{IHT}} = 0$). The lack of perfect fit in Figure 2C may suggest that the material parameters (D, k_1, k_2, k_3, χ) might be slightly different at ETM and HTM sides, and it is better to make the global fit for the excitation from only one side (preferably at several pump fluences). We recently proposed a way to measure the transient absorption of PSCs through the metal electrodes and, thus, under applied voltage [32]. In that previous work, we showed the effect of forward V_{OC} bias at relatively high fluence, so the changes in the kinetics due to the influence of k_{IET} were small (e.g., residual signal relative change of about 5% between 0 V and V_{OC} bias, Figure 2A). For the current work, we made new PSCs and repeated the analogous measurements under a lower pump fluence at which the influence of k_{IET} is more pronounced (residual signal change of about 18%; Figure 2B). In both cases (Figure 2A,B), our assumptions are supported by good model fits. Furthermore, we also tested the influence of different forward biases and found that the value of the applied voltage around V_{OC} is not critical—in our case, the *BI* kinetics were similar between −900 and −1200 mV (Figure S5).

Finally, the interesting effects of diffusion coefficient variation can be pointed out (Figure S4A–C). When D increases from 0 to 0.02 cm^2/s, the charge population decay becomes faster, because more charges are injected. However, further increase in D (up to the simulated values of 2 cm^2/s) results in slower decay in the 3 ns time window, because electrons and holes are spreading faster over the perovskite volume and the probability of second- and third-order recombination decreases.

The above model has discrete boundary conditions (delta functions) that open the electron or hole injection channels at 1 nm distance from the contacts with ETM ($z = 0$) or HTM ($z = L$), respectively. The charge injections rate constants (k_{IET}, k_{IHT}) have, then, the experimental units of s^{-1}, identical to k_1. In the model without diffusion, it is a reasonable way to introduce the charge injection on the boundary. However, arbitrarily choosing of the injection range is required, which, when changing its value, leads to the change in the injection rate constant. The use of diffusion enables a natural way for the implementation of interfacial charge transfer using the boundary conditions. This approach does not allow any arbitrary assumptions. Therefore, the boundary conditions should take the form of the following equations [34,35]:

$$D\frac{\partial n_{\text{e}}}{\partial z}\bigg|_{z=0} = S_{\text{IET}} n_{\text{e}}; \quad D\frac{\partial n_{\text{h}}}{\partial z}\bigg|_{z=L} = -S_{\text{IHT}} n_{\text{h}}, \tag{12}$$

where parameters S_{IET} and S_{IHT} have the units of cm/s and can be called the speed of electron and hole injection, respectively. The relation between the parameters can be calculated from formula $S_{\text{IET/IHT}} = k_{\text{IET/IHT}} \times \text{width of } \delta_{\text{e/h}}(z) \text{ area} = k_{\text{IET/IHT}} \times 10^{-7}\text{cm}$. We tested the above correction and we found that both approaches (discrete and continuous) are in agreement (Figure S6). The implementation of the boundary conditions is presented in SI.

3. Materials and Methods

3.1. Sample Preparation

The preparation protocol followed that published by Saliba et al. [45]. Plates of the size 2.4 × 2.4 cm of FTO (fluorine-doped tin oxide) substrates (FTO glass, ≈13 Ω/sq, Sigma-Aldrich, Merck KGaA, Darmstadt, Germany) were cut, and part of the FTO conductive layer was etched by Zn powder and HCl to prevent charge recombination between gold electrodes and FTO. The etched substrates were brushed with detergent (Hellmanex, Hellma, Germany) and then bathed in detergent, distilled water, and isopropanol in ultrasounds, each step of 15 min. Finally, a UV ozone cleaner was used for 15 min. A compact TiO_2 layer was deposited by spray pyrolysis at 450 °C using titanium diisopropoxide in ethanol (1:14 v/v in EtOH) as a precursor solution. A mesoporous titania layer was obtained by deposition of titania paste (30NR-D, GreatCell Solar, Queanbeyan East, Australia, diluted 1:6 w/w in EtOH) by spin coating (10 s, 2000 rpm) and annealing the substrate at 500 °C for 30 min. $FAPbI_3/MAPbBr_3/CsI$ precursor solutions were prepared in glovebox conditions (in nitrogen flux) and mixed to obtain a 1.5 M precursor solution of the $FA_{0.76}MA_{0.19}Cs_{0.05}Pb(I_{0.81}Br_{0.19})_3$ perovskite. The solution was spin-coated on a mesoporous layer in a dry box with an additional nitrogen flow for 10 s at 2000 rpm and then for 20 s at 4000 rpm; 10 s before the end of this process, chlorobenzene as an anti-solvent was used. A solution of 2,2′,7,7′-tetrakis-(N,N-di-4methoxyphenylamino)-9,9′-spirobifluorene (Spiro-OMeTAD, Sigma-Aldrich) (72.3 mg/mL in chlorobenzene) with additives (17.5 µL/mL of a 520 mg/mL LiTFSI solution in acetonitrile and 28.8 µL/mL *4-tert*-buthylpyridine) was also spin-coated (4000 rpm, 30 s). Finally, 70 nm gold electrodes were sputtered on the top.

3.2. Transient Absorption

Femtosecond transient absorption spectroscopy studies were performed on a 1 kHz repetition rate and a 0.4 ps response function setup delivered by Ultrafast Systems (Spectra-Physics laser system, Santa Clara, CA, USA, and Helios spectrometer, Sarasota, FL, USA) [32]. Measurements were performed in the Vis-NIR (500–850 nm) region, with a 475 nm or 495 nm excitation wavelength, in the temporal window of up to 3 ns. Additional bias during transient absorption measurement was applied to the electrodes by a compact potentiostat (model PGSTAT204, Metrohm Autolab, Utrecht, The Netherlands).

3.3. Numerical Simulations

Simulations were performed in COMSOL Multiphysics software (version 5.4). In addition, 1D geometry was used. The perovskite layer was added as an Interval from 0 to L. In the Physics interface, Coefficient Form PDE from the Mathematics module was used to implement Equations (7) and (8), solving two dependent variables n_e and n_h. The implementation consisted of the following parameters defined in Coefficient Form PDE:

$$c = \begin{pmatrix} D & 0 \\ 0 & D \end{pmatrix},$$

$$a = \begin{pmatrix} k_1 + k_2 n_\mathrm{h} + k_3 n_\mathrm{e} n_\mathrm{h} + k_\mathrm{IET}\delta_\mathrm{e}(z) & 0 \\ 0 & k_1 + k_2 n_\mathrm{e} + k_3 n_\mathrm{e} n_\mathrm{h} + k_\mathrm{IHT}\delta_\mathrm{h}(z) \end{pmatrix},$$

$$d_a = \begin{pmatrix} 1 & 0 \\ 0 & 1 \end{pmatrix}.$$

The remaining parameters were equal to zero. δ_e and δ_h were implemented using the Step function. The initial distribution of charges was implemented in Initial Values as $n_\mathrm{e} = n_0\exp(-\alpha z)$ $[n_0\exp(-\alpha(L-z))]$ and $n_\mathrm{h} = n_0\exp(-\alpha z)$ $[n_0\exp(-\alpha(L-z))]$ for the excitation from the ETM (HTM) side. The mesh with the element size of 0.05 nm was used. Simulations were performed using a Time Dependent study with predefined settings. The simulation data were collected from 1 ps to 3 ns using the logarithmic step with 50 steps per decade.

The boundary conditions defined in Equation (12) were implemented in Coefficient Form PDE using the Flux/Source function. Here, parameter S_IET was implemented as

$$q = \begin{pmatrix} S_\mathrm{IET} & 0 \\ 0 & 0 \end{pmatrix}$$

at the boundary placed at $z = 0$ and S_{IHT} as

$$q = \begin{pmatrix} 0 & 0 \\ 0 & S_{\mathrm{IHT}} \end{pmatrix}$$

at the boundary placed at $z = L$, while term p was equal to zero. The constants used in the study ($k_1, k_2, k_3, k_{\mathrm{IET}}, k_{\mathrm{IHT}}, D, n_0, \alpha, L, \chi, S_{\mathrm{IET}}, S_{\mathrm{IHT}}$) were defined in Global Definitions as Parameters.

4. Conclusions

In conclusion, we propose a simple mathematical model and methodology for the extraction of correct values of the parameters that govern charge transfers in complete PSCs on ultrafast and fast time scales (ps–ns). We refine the existing approaches and show the necessity of including the charge diffusion and both second- and third-order charge recombination processes in the interpretation of electron and hole population kinetics. Broadband analysis of transient absorption data is also required. For sufficiently short-wavelength excitation and the perovskite layer thickness typical for complete cells (>500 nm), the charge injection at only one (incident) interface is important (perovskite/ETM or perovskite/HTM). The contribution of electron or hole injection can be most easily observed at low excitation fluences (<5 μJ/cm^2) by comparing the data with and without the applied bias voltage. We believe that our work will pave the way for more properly analyzed time-resolved studies of the interfaces between perovskites and selective contact materials leading to a better understanding of the factors that influence the efficiency of PSCs.

Supplementary Materials: The following supporting information can be downloaded at: https://www.mdpi.com/article/10.3390/ma16227110/s1, Figure S1: (A) Schematic presentation of the formation of the bleach (blocked transition) at the low-energy edge of absorption in perovskite after charge cooling, and the reduction of bleach after either electron transfer to ETM or hole transfer to HTM due to the delocalization of the charges. (B) Pseudo-color 2D spectra of original transient absorption data corresponding to higher pump fluence excited from ETM side in Figure 2C. Figure S2: Simulation of the distribution of the electrons and holes along perovskite thickness at different times after excitation from the ETM side for low and high pump fluence. Figure S3: Simulations of charge population decay observed in transient absorption of PSCs (calculated from Equation (10)) for different parameters variation (χ, k_1, k_2, k_3). Figure S4: Simulations of charge population decay observed in transient absorption of PSCs (calculated from Equation (10)) for different parameters variation (D, k_{IET}, k_{IHT}, L). Figure S5: Averaged residual *BI* signal for a different applied voltage of PSC excited from ETM side with 475 nm pump pulse of 2.3 μJ/cm^2. Figure S6: The comparison between two approaches of interface charge transfer implementation—using delta functions in the vicinity of the boundary (solid lines) and using boundary conditions for the gradient of the charge population (dashed lines) for three values of k_{IET} and S_{IET}.

Author Contributions: Conceptualization, K.S. and M.Z.; methodology, K.S. and K.P.-B.; software, K.S.; validation, K.S. and K.P.-B.; investigation, K.S., K.P.-B. and M.Z.; data curation, K.S., K.P.-B. and M.Z.; writing—original draft preparation, K.S., K.P.-B. and M.Z.; writing—review and editing, K.S., K.P.-B. and M.Z. All authors have read and agreed to the published version of the manuscript.

Funding: K.S. acknowledges the financial support from the Foundation for Polish Science (FNP), grant no. START 082.2022.

Institutional Review Board Statement: Not applicable.

Informed Consent Statement: Not applicable.

Data Availability Statement: The data presented in this study are available on request from the corresponding author.

Acknowledgments: Maciej Krawczyk (Institute of Spintronics and Quantum Information, Faculty of Physics, Adam Mickiewicz University) is kindly acknowledged for his assistance in establishing the scientific cooperation and sharing the calculation resources of his research group.

Conflicts of Interest: The authors declare no conflict of interest.

References

1. National Renewable Energy Laboratory Best Research Cell Efficiencies Chart. Available online: https://www.nrel.gov/pv/cell-efficiency.html (accessed on 6 June 2023).
2. Nishida, J.; Chang, P.T.S.; Ye, J.Y.; Sharma, P.; Wharton, D.M.; Johnson, S.C.; Shaheen, S.E.; Raschke, M.B. Nanoscale Heterogeneity of Ultrafast Many-Body Carrier Dynamics in Triple Cation Perovskites. *Nat. Commun.* **2022**, *13*, 6582. [CrossRef] [PubMed]
3. Marchioro, A.; Teuscher, J.; Friedrich, D.; Kunst, M.; Van De Krol, R.; Moehl, T.; Grätzel, M.; Moser, J.E. Unravelling the Mechanism of Photoinduced Charge Transfer Processes in Lead Iodide Perovskite Solar Cells. *Nat. Photonics* **2014**, *8*, 250–255. [CrossRef]
4. Yang, Y.; Yang, M.; Moore, D.T.; Yan, Y.; Miller, E.M.; Zhu, K.; Beard, M.C. Top and Bottom Surfaces Limit Carrier Lifetime in Lead Iodide Perovskite Films. *Nat. Energy* **2017**, *2*, 16207. [CrossRef]
5. Brauer, J.C.; Tsokkou, D.; Sanchez, S.; Droseros, N.; Hua, X.; Stolterfoht, M.; Neher, D.; Roose, B.; Steiner, U.; De Angelis, F. Comparing the Excited-State Properties of a Mixed-Cation—Mixed-Halide Perovskite to Methylammonium Lead Iodide. *J. Chem. Phys.* **2020**, *152*, 104703. [CrossRef]
6. Shen, Q.; Ogomi, Y.; Chang, J.; Tsukamoto, S.; Kukihara, K.; Oshima, T.; Osada, N.; Yoshino, K.; Katayama, K.; Toyoda, T.; et al. Charge Transfer and Recombination at the Metal Oxide/$CH_3NH_3PbClI_2$/Spiro-OMeTAD Interfaces: Uncovering the Detailed Mechanism behind High Efficiency Solar Cells. *Phys. Chem. Chem. Phys.* **2014**, *16*, 19984–19992. [CrossRef]
7. Ponseca, C.S.; Hutter, E.M.; Piatkowski, P.; Cohen, B.; Pascher, T.; Douhal, A.; Yartsev, A.; Sundstrom, V.; Savenije, T.J. Mechanism of Charge Transfer and Recombination Dynamics in Organo Metal Halide Perovskites and Organic Electrodes, PCBM, and Spiro-OMeTAD: Role of Dark Carriers. *J. Am. Chem. Soc.* **2015**, *137*, 16043–16048. [CrossRef]
8. Navedu, M.; Apurba, D.; Sumanta, P.; Anunay, S. Ultrafast Carrier Dynamics of Metal Halide Perovskite Nanocrystals and Perovskite-Composites. *Nanoscale* **2019**, *11*, 9796–9818. [CrossRef]
9. Jiang, Q.; Tong, J.; Xian, Y.; Kerner, R.A.; Dunfield, S.P.; Xiao, C.; Scheidt, R.A.; Kuciauskas, D.; Wang, X.; Hautzinger, M.P.; et al. Surface Reaction for Efficient and Stable Inverted Perovskite Solar Cells. *Nature* **2022**, *611*, 278–283. [CrossRef]
10. Giordano, F.; Abate, A.; Pablo, J.; Baena, C.; Saliba, M.; Matsui, T.; Im, S.H.; Zakeeruddin, S.M.; Nazeeruddin, M.K.; Hagfeldt, A.; et al. Enhanced Electronic Properties in Mesoporous TiO_2 via Lithium Doping for High-Efficiency Perovskite Solar Cells. *Nat. Commun.* **2016**, *7*, 10379. [CrossRef]
11. Kirchartz, T. Picturing Charge Carrier Diffusion. *Nat. Mater.* **2022**, *21*, 1344–1345. [CrossRef]
12. Stranks, S.D.; Eperon, G.E.; Grancini, G.; Menelaou, C.; Alcocer, M.J.P.; Leijtens, T.; Herz, L.M.; Petrozza, A.; Snaith, H.J. Electron-Hole Diffusion Lengths Exceeding 1 Micrometer in an Organometal Trihalide Perovskite Absorber. *Science* **2013**, *342*, 341–344. [CrossRef]
13. Xing, G.; Mathews, N.; Sun, S.; Lim, S.S.; Lam, Y.M.; Graẗzel, M.; Mhaisalkar, S.; Sum, T.C. Long-Range Balanced Electron-and Hole-Transport Lengths in Organic-Inorganic $CH_3NH_3PbI_3$. *Science* **2013**, *342*, 344–347. [CrossRef] [PubMed]
14. Herz, L.M. Charge-Carrier Dynamics in Organic-Inorganic Metal Halide Perovskites. *Annu. Rev. Phys. Chem.* **2016**, *67*, 65–89. [CrossRef] [PubMed]
15. Crothers, T.W.; Milot, R.L.; Patel, J.B.; Parrott, E.S.; Schlipf, J.; Müller-Buschbaum, P.; Johnston, M.B.; Herz, L.M. Photon Reabsorption Masks Intrinsic Bimolecular Charge-Carrier Recombination in $CH_3NH_3PbI_3$ Perovskite. *Nano Lett.* **2017**, *17*, 5782–5789. [CrossRef] [PubMed]
16. Leng, J.; Liu, J.; Zhang, J.; Jin, S. Decoupling Interfacial Charge Transfer from Bulk Diffusion Unravels Its Intrinsic Role for Efficient Charge Extraction in Perovskite Solar Cells. *J. Phys. Chem. Lett.* **2016**, *7*, 5056–5061. [CrossRef] [PubMed]
17. Serpetzoglou, E.; Konidakis, I.; Kakavelakis, G.; Maksudov, T.; Kymakis, E.; Stratakis, E. Improved Carrier Transport in Perovskite Solar Cells Probed by Femtosecond Transient Absorption Spectroscopy. *ACS Appl. Mater. Interfaces* **2017**, *9*, 43910–43919. [CrossRef] [PubMed]
18. Pydzińska, K.; Karolczak, J.; Kosta, I.; Tena-Zaera, R.; Todinova, A.; Idígoras, J.; Anta, J.A.; Ziółek, M. Determination of Interfacial Charge-Transfer Rate Constants in Perovskite Solar Cells. *ChemSusChem* **2016**, *9*, 1647–1659. [CrossRef]
19. Scholz, M.; Flender, O.; Oum, K.; Lenzer, T. Pronounced Exciton Dynamics in the Vacancy-Ordered Bismuth Halide Perovskite $(CH_3NH_3)_3Bi_2I_9$ Observed by Ultrafast UV-Vis-NIR Transient Absorption Spectroscopy. *J. Phys. Chem. C* **2017**, *121*, 12110–12116. [CrossRef]
20. Wang, L.; McCleese, C.; Kovalsky, A.; Zhao, Y.; Burda, C. Femtosecond Time-Resolved Transient Absorption Spectroscopy of $CH_3NH_3PbI_3$ Perovskite Films: Evidence for Passivation Effect of PbI_2. *J. Am. Chem. Soc.* **2014**, *110*, 12205–12208. [CrossRef]
21. Pydzińska-Białek, K.; Szeremeta, J.; Wojciechowski, K.; Ziółek, M. Insights into the Femtosecond to Nanosecond Charge Carrier Kinetics in Perovskite Materials for Solar Cells. *J. Phys. Chem. C* **2019**, *123*, 110–119. [CrossRef]
22. Pydzińska, K.; Drushliak, V.; Coy, E.; Załęski, K.; Flach, J.; Idígoras, J.; Contreras-Bernal, L.; Hagfeldt, A.; Anta, J.A.; Ziółek, M. Understanding the Interfaces between Triple Cation Perovskite and Electron or Hole Transporting Material. *ACS Appl. Mater. Interfaces* **2020**, *12*, 30399–30410. [CrossRef] [PubMed]

23. Zhou, M.; Sarmiento, J.S.; Fei, C.; Wang, H. Charge Transfer and Diffusion at the Perovskite/PCBM Interface Probed by Transient Absorption and Reflection. *J. Phys. Chem. C* **2019**, *123*, 22095–22103. [CrossRef]
24. Droseros, N.; Dänekamp, B.; Tsokkou, D.; Boix, P.P.; Banerji, N. Charge Injection and Trapping at Perovskite Interfaces with Organic Hole Transporting Materials of Different Ionization Energies. *APL Mater.* **2019**, *7*, 041115. [CrossRef]
25. Shen, W.; Wu, Z.; Yang, G.; Kong, Y.; Li, W.; Liang, G.; Huang, F.; Cheng, Y.; Zhong, J. Differentiated Functions of Potassium Interface Passivation and Doping on Charge-Carrier Dynamics in Perovskite Solar Cells. *J. Phys. Chem. Lett.* **2022**, *13*, 3188–3193. [CrossRef]
26. Li, C.; Wang, A.; Deng, X.; Wang, S.; Yuan, Y.; Ding, L.; Hao, F. Insights into Ultrafast Carrier Dynamics in Perovskite Thin Films and Solar Cells. *ACS Photonics* **2020**, *7*, 1893–1907. [CrossRef]
27. Yan, L. Ultrafast Photoinduced Carrier Dynamics in Single Crystalline Perovskite Films. *J. Mater. Chem. C* **2023**, *11*, 3736–3742. [CrossRef]
28. Pydzińska-Białek, K.; Glinka, A.; Drushliak, V.; Nowaczyk, G.; Florczak, P.; Ziółek, M. Impact of Improvements in Mesoporous Titania Layers on Ultrafast Electron Transfer Dynamics in Perovskite and Dye-Sensitized Solar Cells. *Phys. Chem. Chem. Phys.* **2020**, *22*, 21947–21960. [CrossRef]
29. Handa, T.; Tex, D.M.; Shimazaki, A.; Wakamiya, A.; Kanemitsu, Y. Charge Injection Mechanism at Heterointerfaces in $CH_3NH_3PbI_3$ Perovskite Solar Cells Revealed by Simultaneous Time-Resolved Photoluminescence and Photocurrent Measurements. *J. Phys. Chem. Lett.* **2017**, *8*, 954–960. [CrossRef]
30. Li, X.; Bi, D.; Yi, C.; Décoppet, J.-D.; Luo, J.; Zakeeruddin, S.M.; Hagfeldt, A.; Grätzel, M. A Vacuum Flash-Assisted Solution Process for High-Efficiency Large-Area Perovskite Solar Cells. *Science* **2016**, *353*, 58–62. [CrossRef]
31. Quere, B.; Pydzińska-Białek, K.; Karolczak, J.; Nowaczyk, G.; Coy, E.; Ziółek, M. Understanding the Effect of Different Synthesis Conditions on the Physicochemical Properties of Mixed-Ion Perovskite Solar Cells. *Chem. A Eur. J.* **2019**, *25*, 5978–5986. [CrossRef]
32. Pydzińska-Białek, K.; Nowaczyk, G.; Ziółek, M. Complete Perovskite Solar Cells with Gold Electrodes Studied in the Visible and Near-Infrared Ranges. *Chem. Mater.* **2022**, *34*, 6355–6366. [CrossRef]
33. Brauer, J.C.; Lee, Y.H.; Nazeeruddin, M.K.; Banerji, N. Charge Transfer Dynamics from Organometal Halide Perovskite to Polymeric Hole Transport Materials in Hybrid Solar Cells. *J. Phys. Chem. Lett.* **2015**, *6*, 3675–3681. [CrossRef] [PubMed]
34. Gao, Y.; Liu, J.; Isikgor, F.H.; Wang, M.; Khan, J.I.; Wolf, S. De Probing Ultrafast Interfacial Carrier Dynamics in Metal Halide Perovskite Films and Devices by Transient Reflection Spectroscopy. *ACS Appl. Mater. Interfaces* **2022**, *14*, 34281–34290. [CrossRef] [PubMed]
35. Staub, F.; Anusca, I.; Lupascu, D.C.; Rau, U.; Kirchartz, T. Effect of Reabsorption and Photon Recycling on Photoluminescence Spectra and Transients in Lead-Halide Perovskite Crystals. *J. Phys. Mater.* **2020**, *3*, 025003. [CrossRef]
36. Kovalenko, S.A.; Schanz, R.; Farztdinov, V.M.; Hennig, H.; Ernsting, N.P. Femtosecond Relaxation of Photoexcited Para-Nitroaniline: Solvation, Charge Transfer, Internal Conversion and Cooling. *Chem. Phys. Lett.* **2000**, *323*, 312–322. [CrossRef]
37. Dong, C.; Wang, Z.K.; Liao, L.S. Progress of Triple Cation Organometal Halide Perovskite Solar Cells. *Energy Technol.* **2020**, *8*, 1–14. [CrossRef]
38. Yaiche, A.; Sha, H.; Cacovich, S.; Messou, D.; Bercegol, A.; Rousset, J.; Schulz, P.; Bouttemy, M.; Lombez, L. Light-Induced Passivation in Triple Cation Mixed Halide Perovskites: Interplay between Transport Properties and Surface Chemistry. *ACS Appl. Mater. Interfaces* **2020**, *12*, 34784–34794. [CrossRef]
39. Krückemeier, L.; Krogmeier, B.; Liu, Z.; Rau, U.; Kirchartz, T. Understanding Transient Photoluminescence in Halide Perovskite Layer Stacks and Solar Cells. *Adv. Energy Mater.* **2021**, *11*, 2003489. [CrossRef]
40. Krogmeier, B.; Staub, F.; Grabowski, D.; Rau, U.; Kirchartz, T. Quantitative Analysis of the Transient Photoluminescence of $CH_3NH_3PbI_3/PC_{61}BM$ Heterojunctions by Numerical Simulations. *Sustain. Energy Fuels* **2018**, *2*, 1027–1034. [CrossRef]
41. Burkhard, B.G.F.; Hoke, E.T.; Mcgehee, M.D. Accounting for Interference, Scattering, and Electrode Absorption to Make Accurate Internal Quantum Efficiency Measurements in Organic and Other Thin Solar Cells. *Adv. Mater.* **2010**, *94305*, 3293–3297. [CrossRef]
42. Kar, S.; Kaushal, K.; Yantara, N.; Mhaisalkar, S.G. Optical Simulations in Perovskite Devices: A Critical Analysis. *ACS Photonics* **2022**, *9*, 3196–3214. [CrossRef]
43. Richardson, G.; Foster, J.M. How Transport Layer Properties Affect Perovskite Solar Cell Performance: Insights from a Coupled Charge Transport / Ion Migration Model. *Energy Environ. Sci.* **2019**, *12*, 396–409. [CrossRef]
44. Singh, A.; Kaiser, W.; Gagliardi, A. Role of Cation-Mediated Recombination in Perovskite Solar Cells. *Sol. Energy Mater. Sol. Cells* **2021**, *221*, 110912. [CrossRef]
45. Saliba, M.; Wol, C.M.; Stolterfoht, M.; Phung, N.; Albrecht, S.; Neher, D.; Abate, A. How to Make over 20% Efficient Perovskite Solar Cells in Regular (n–i–p) and Inverted (p–i–n) Architectures. *Chem. Mater.* **2018**, *30*, 4193–4201. [CrossRef]